Application of Automated Iterative Target Detection for Standoff Hyperspectral Imaging

Brenda M. Forland, Neal B. Gallagher, and Timothy J. Johnson

***Abstract*—The utility of hyperspectral imaging (HSI) has been well established for a wide array of applications but has generated a need for automated screening of high volumes of large HSI cubes. We report two important automated algorithms for efficient standoff processing: atmospheric compensation and target detection. The atmospheric compensation method is based on a fast asymmetric least squares approach that is applied on a pixel-by-pixel basis. The compensation can be applied to entire images without manually identifying regions of interest and utilizes only in-scene information; no ancillary modeling of the atmosphere is required. An iterative target detection approach is also introduced which demonstrates faster speeds relative to moving window approaches. The target detection algorithm classifies each pixel as true target detections, near target detections, clutter, and no-calls. The algorithms were tested using longwave infrared data (7.7 - 11.7 µm) on forty images of twenty-four solid and powder mineral targets placed at a 14-meter standoff distance allowing general observations on expected detection performance for a variety of minerals. In addition to identifying anomalous pixels, the inclusion of "no-calls" significantly reduced the number of false detections.**

***Index Terms*—automated, background, clutter, extended least squares, generalized least squares, hyperspectral imaging, iterative, target detection, principal component analysis**

Brenda M. Forland and Timothy J. Johnson were supported by Pacific Northwest National Laboratory, which is managed for the US Department of Energy by Battelle under contract DE-AC05-76RL01830. *(Corresponding author: Brenda M. Forland).*

Brenda M. Forland is with Pacific Northwest National Laboratory, Richland, WA 99352 (e-mail: Brenda.Forland@pnnl.gov).

Neal B. Gallagher is with Eigenvector Research, Inc, Manson, WA 98831 (e-mail: nealg@eigenvector.com).

Timothy J. Johnson is with Pacific Northwest National Laboratory, Richland, WA 99352 (e-mail: Timothy.Johnson@pnnl.gov).

I. INTRODUCTION

In hyperspectral imaging (HSI), target detection is often defined as the ability to discriminate the presence of target spectral signatures from background clutter [1-6]. HSI detection has found application at identifying defect signatures on surfaces, adulterants in raw materials and food [7], but also in forensics, medical imaging and remote sensing. Because of the many impressive achievements, HSI has grown in popularity and applications, but the need for fully automated screening and analysis / clutter suppression has grown with it. As the need for better and faster algorithms grows, e.g. for onboard/onsite processing, the present work represents an attempt towards that end. Clutter is defined as spectral interference not associated with the target signal, arising from the highly varied spatial distributions in naturally occurring scenes [8-10]. This work details progress on two automated tools, both applicable to target detection and clutter suppression at standoff distances via analysis of HSI data measured in the longwave infrared with a 7.7 - 11.7 µm Telops instrument. The approach is a two-step process including atmospheric

compensation followed by target detection [11]. The atmospheric compensation of the first step includes a temperature-emissivity separation, allowing the second step to better utilize known library reflectance spectra for target detection. This pipeline can be applied automatically to images measured in radiance without the time- and labor-intensive need for humans to identify spatial or spectral regions of interest, highlighting the full analysis pathway from data collection to target detection.

A. Atmospheric Compensation

Early imagers often had only a few channels, but as technology has improved and computing power has grown, hyperspectral imagers have come into form [12-14] with hundreds of spectral bands, and higher spectral resolution across the visible and near-infrared (VNIR), shortwave (SWIR), and longwave infrared (LWIR) domains. In the present analysis, LWIR radiance cubes were converted to reflectance via atmospheric compensation and temperature-emissivity separation as first steps followed by target detection performed in reflectance mode using library reflectance spectra. Converting at-sensor radiance to emissivity (or reflectance) in the longwave infrared (LWIR) region does in fact require two steps, namely atmospheric compensation followed by temperature emissivity separation (TES) [15][16]. This is because downstream applications such as target detection have greater efficacy on atmospherically corrected data than simple calibrated radiance, hence the importance of these processing steps [17]. Particularly in the LWIR [18][19], there can be significant variability present in a measured HSI data set, and effects such as radiative transfer, topography, morphology, adjacency, etc., make it difficult to estimate reflectance from radiance [9][20]. Moreover, atmospheric effects, illumination, acquisition geometry, adjacent environmental materials and the sensor's own response can all cause spectral variability of the radiance registered by the sensor [9][11][21][22].

For atmospheric compensation in the LWIR, multiple approaches exist: One method is to use in-scene information. In-Scene Atmospheric Compensation (ISAC) assumes negligible downwelling radiation and exploits the linearity of the remaining terms in the observed radiance, fitting lines for each band. Each band is properly scaled to compensate for the effect of the atmosphere on the brightness temperature in a linear fashion where the gain is atmospheric transmission and offset is upwelling. This approach assumes some pixels are simple blackbodies. Scaling in the LWIR utilizes the 11.7 μm water band [15-18][23][24]. Autonomous Atmospheric Compensation (AAC) similarly assumes the downwelling is negligible and utilizes the water band at 11.7 μm [17][24]. Emissive Empirical Line Method (EELM) utilizes presence of calibration targets for which emissivity and temperature are well known and utilizes linear regression for each band; EELM is an extension of the Empirical Line Method (ELM) used in the VNIR and SWIR domains [16]. Other approaches that employ a modeling approach create atmospheric models of the atmospheric terms, such as via use of a database, or more explicitly via use of Moderate Resolution Atmospheric Transmission (MODTRAN), a radiative transfer modeling program [21][24][25]. For scenes focused on visible to mid-wave, other approaches such as ATCOR, QUAC, or FLAASH are quite common [21][26-33]. Depending on the sensing scenario, the algorithms each make certain assumptions. For this work, we focus on a ground-based sensor and assume the upwelling term is negligible.

Once an LWIR scene has been atmospherically compensated, the scene must undergo a temperature emissivity separation (TES) to allow estimation of reflectance used in target detection. For the TES, a range of options have been employed. For an image with N spectral bands, however, the challenge is that there exist $N + 1$ unknowns (emissivity for each band and the temperature) and only N knowns (the at-sensor radiance for each band), making it an underdetermined problem [11][15][18][24][29]. Normalized Emissivity Method (NEM) is one approach to solving the TES predicament [16-18] and is based on an assumption of an emissivity for a spectral band for maximum brightness temperature [15]. The band with maximum temperature is assigned the assumed emissivity and the temperature is then used to derive emissivity values for the remaining bands in that pixel [15]. The Planck-

Modeled Temperature Emissivity Separation (PM-TES) does not require such an assumption; instead it uses in-scene statistics and identifies a temperature modulated region by investigating chi-squared statistics of spatially proximal pixels, then models the Planck function over a range of temperature and emissivity, hopefully capturing modeled ranges and thereby finding the ratios of emissivity for all wavelength combinations [15]. The MCMC-TES algorithm is a Bayesian approach using Markov chain Monte Carlo methods; it employs Gibbs sampling techniques that calculate prior distributions from an emissivity database and thus provide uncertainty of the estimations in the posterior [34]. ARTEMISS uses a boxcar moving average filter approach whereby the linear emissivity constraint (LEC) TES utilizes a piecewise linear approximation of emissivity [11]. An alternative approach to automating the TES involves principal component analysis (PCA) [35][36]. PCA reduces dimensions and thus helps circumvent the N knowns / $N + 1$ unknowns dilemma [24].

Some of the more modern approaches combine the atmospheric compensation and the TES into a single automated software: Fast Line-of-sight Atmospheric Analysis of Spectral Hypercubes – Infrared (FLAASH-IR) is one such algorithm [29]. FLAASH-IR takes a smoothness approach and minimizes the sigma squared between the computed radiance and observed data. The algorithm then uses this minimum to derive the atmospheric parameters from the scene to modify a MODTRAN model and determine the TES [29]. This approach works well for low emissivity materials as well, outperforming other approaches in this category [29]. In this paper, we introduce a new approach for LWIR datacubes which uses an asymmetric least-squares scene-based atmospheric compensation algorithm. For this work, the highest brightness temperature was used to provide and estimate for TES. The method uses only in-scene measurements for compensation, avoids atmospheric modeling, and extracts estimates of reflectance (a unique property of the analyte). The approach introduced here is applicable to standoff imaging and provides a fast compensation scheme that is not influenced by potential atmospheric modeling errors, resulting in a good first order compensation. Details of the atmospheric compensation algorithm are provided below. In essence, the algorithm accounts for reflected downwelling sky radiance followed by a temperature-emissivity separation approximation.

B. Target Detection

A popular target detection algorithm known as the generalized least squares (GLS) estimator was introduced [37] by C. Aitken and is also known as a matched filter [38], generalized likelihood ratio test [1][3][6], or simply GLS [20][39-40]. There are many target detection approaches but the focus of target detection in this paper is the spectral matched filter (generalized least squares) because it is well known, simple to apply, sensitive, and designed for sub-pixel detection. Many additional approaches such as the adaptive cosine estimator, spectral angle mapper, spectral correlation mapper, target constrained interference minimized filter, kernel-based methods, etc. have been employed and are discussed in references [1-4][41-43]. A distinct advantage of the GLS estimator, however, is that it provides both full pixel (target occupies the entire pixel) and sub-pixel detection (where target and clutter are both included in the same pixel signal). GLS is typically used as a binary classifier indicating that a target is either "detected" or "not detected" in any given pixel. In contrast, the work presented here classifies pixels into four classes: detected target signal, possible detections, clutter signal (non-detections), and "no-calls". No-calls are based on a model error statistic and are considered anomalous pixels that should be considered neither a detection nor a typical clutter signal. The proposed algorithm uses a replacement model [9] that incorporates both GLS and extended least squares (ELS) [40]. ELS is directly related to orthogonal subspace projection (first introduced by Harsanyi and Chang [44]), orthogonal background subtraction [45], extended mixture modeling [46], and external parameter orthogonalization [47]. The replacement model is consistent with commonly used

endmember extraction methods [8] and is consistent with an important reduction of Hapke's reflectance model [22] provided in [8].

Recently, deep learning and machine learning are also utilized for target detection. Deep learning has been shown to improve performance in the LWIR where temperature changes make target detection more difficult due thermal radiation being the dominant contributor to the signal. Using a generative adversarial network to convert the scene with unknown temperature to a scene with known temperature improves target detection performance with the use of a multi-scale 3D deep convolutional neural network [48]. Neural networks have also been shown to outperform ACE in both radiance and emissivity space for LWIR [49]. Similar success has been found in scenes that are in the visible-near and short-wave infrared regions, where transformers have been used to capture the spatial-spectral relationship [50]. The lack of training data is a concern for data hungry networks and investigations into the use of synthetic data [49][51].

Global clutter models assume that the target is a rare feature (appearing only in a few pixels), where the clutter covariance is not significantly affected by target signal. The approach presented here does not classify clutter *a priori* but relies on the principle that detection sensitivity improves when pixels used to estimate the clutter covariance do not include target signal. Each pixel in an image can thus be envisioned as being embedded in clutter with the detection algorithm examining each pixel one-at-a-time. The pixel under examination is referred to as the Pixel-Under-Test (PUT). Windowed detection approaches assume that the clutter is spatially local to the PUT and evaluates each pixel one-at-a-time; a computationally intensive and slow process [3][4]. Other approaches include clustering, which partitions the image into spectrally contiguous clusters of similar clutter [52]. With partitioning algorithms, the method assumes the clutter is more homogenous with fewer clutter sources that need to be accounted for in each cluster, resulting in a more sensitive detection algorithm. The approach used here is an iterative algorithm that avoids windowing. The approach is expected to be especially useful when applied to clusters identified in the partitioning algorithms, but can also be applied to full, non-partitioned images as demonstrated below. The algorithm uses an initial low detection threshold (e.g., at an 80% confidence limit) and pixels with potential detections are removed from the clutter model iteratively until new detections are not found. After the iteration is completed at the low detection threshold, the removed "potential" detections are then tested at a higher detection threshold to find "true" detections. In this work, the iterative approach was applied to full images to demonstrate how the method can be used for screening.

C. Experiment and Analysis

The present method provides an automated methodology for atmospheric compensation and target detection using data from a previously reported HSI measurement campaign [20][53]. Briefly, standoff HSI spectra were recorded for a few solid mineral pieces and dozens of mineral powders, or dry solid chemicals placed in sample cups mounted on a plywood board, the board tilted toward the sensor and positioned at 14 m (45 ft) standoff distance as per [20]. The HSI spectral data were measured in the longwave infrared [7.7 - 11.7 μm, (1270 – 870 cm^{-1})] using a Telops Hypercam sensor at a resolution (FWHM) of 4 cm^{-1} (122 bands) for all the measurements, typically eight datacubes averaged per scan, with four scans averaged to reduce noise. The LWIR Telops has a mercury-cadmium-telluride focal plane array of 320 × 256 pixels with a 350 μrad/pixel using the standard optic; the instrument thus imaged a 1.56 m × 1.25 m scene in object space. The Telops instrument uses internal blackbody references at known temperatures to directly convert the digital signal to radiance [W/(m^2 sr cm^{-1})]. Further experimental details are found in [20]. Example mineral sample cups are seen in Figure 1. The HSI spectra were analyzed using hemispherical reflectance reference data recorded in the laboratory [53], thus demonstrating that HSI data cubes can be successfully exploited using laboratory reference spectra, i.e. without the need for in-scene ground truth measurements. The proposed target detection algorithm compared well vs.

the adaptive cosine estimator (ACE), showing fewer false alarms for a number of scenarios. As seen in Figure 1, the left frame displays a board and samples, while the right frame plots the (laboratory) measured reflectance spectrum of four example mineral powders. Results for these minerals are discussed in detail below.

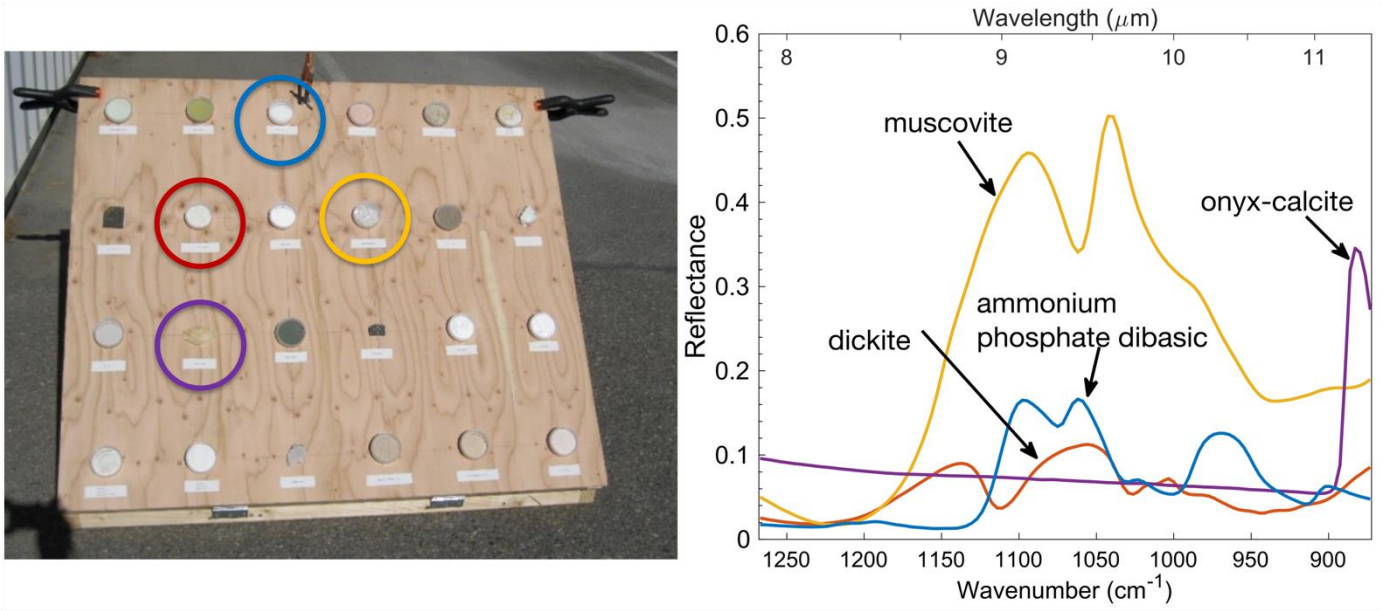

Fig. 1. Example of plywood board with samples (left) and examples of four of the laboratory-measured mineral spectra (right). The colors in the spectral trace plot match colors of circles around the corresponding samples in the photograph.

Previous work [20] performed analysis of the spectra using ROIs (regions of interest) identified by manual target detection. It is noted that target signal does not always perfectly match a given library target spectrum and detected pixels can themselves be used as target signal in further forensics of the image. This is because the detected pixels more closely align to how the target signal manifests in the scene than the library spectrum. Once target pixels are detected using the target detection algorithm, one or more target pixels can be used as targets in a subsequent analysis to detect additional possible target pixels. For example, multiple detected target spectra can be used in whitened principal component analysis [54]. Although not demonstrated here, it is expected that using in-scene targets can provide a more sensitive target detection algorithm.

II. Algorithm Description

Automated target detection analysis of longwave standoff hyperspectral images is a two-step process: The first step described in Section II.A provides atmospheric compensation and temperature-emissivity separation. The input to this algorithm is the measured radiance for an entire image and the output is an image of estimated reflectance, which is passed to the iterative target detection algorithm discussed in Section II.B.

A. Asymmetric Least Squares In-scene Atmospheric Compensation Algorithm

For a passive standoff scenario, the measured radiance $L(\nu)$ at wavenumber ν for a given pixel is modeled as

$$L(\nu) = \Big(\varepsilon(\nu)B(\nu,T) + \big(1-\varepsilon(\nu)\big)L_{\mathrm{d}}(\nu)\Big)\tau(\nu) + L_{\mathrm{u}}(\nu), \qquad (1)$$

where $\varepsilon(\nu)$ is the emissivity of the material contributing to the signal, $B(\nu,T)$ is the Planck blackbody function at temperature T, $L_d(\nu)$ is the downwelling radiance incident on the scene, $\big(1-\varepsilon(\nu)\big)=R(\nu)$ is the sample reflectance using Kirchhoff's law for zero absorptance, $\tau(\nu)$ is the atmospheric transmissivity and $L_{\mathrm{u}}(\nu)$ the upwelling radiance of the atmosphere between the imaged scene and the spectrometer. The terms are illustrated graphically in Figure 2: One must account for the atmospheric upwelling, downwelling, and transmission effects; for these data the upwelling effects are negligible due to the short standoff distances. We also note that the model assumes an isotropic distribution of the reflected light, i.e. a relatively flat BRDF (bidirectional reflection distribution function). While there may be some angles with increased (specular) reflectance for the polished mineral samples, the majority of the samples are powders where an isotropic reflectance distribution can be safely assumed [55-58].

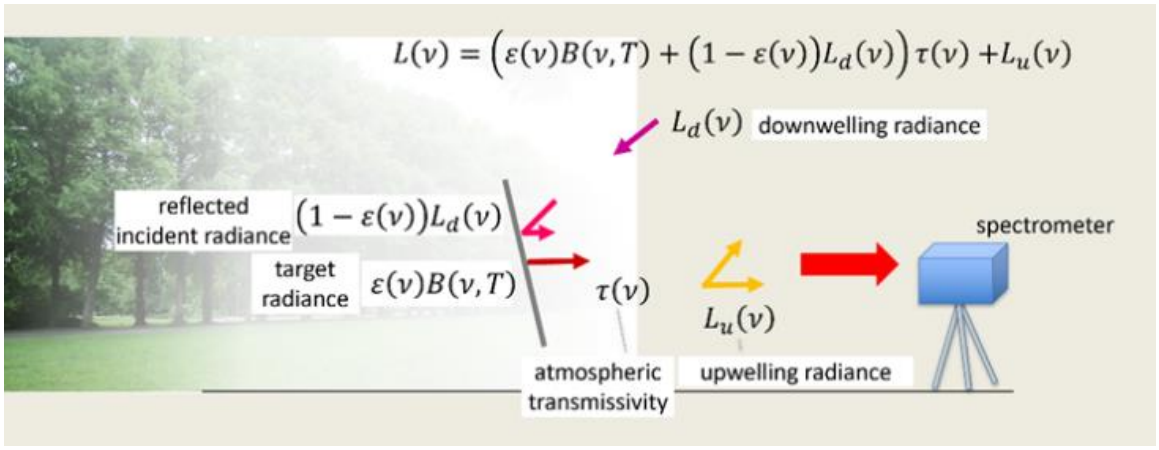

Fig. 2. Depiction of the terms in the equation for measured radiance and the contributing factors. The target radiance is associated with all pixels in an image.

For low humidity conditions at relatively close distances (e.g. < 20 m), $\tau(\nu)\approx 1$ in the spectral windows and $L_u(\nu)\approx 0$, i.e., the upwelling term is negligible since these are short standoff (non-satellite) distances. Equation 1 can thus be approximated as

$$L(\nu)=\varepsilon(\nu)B(\nu,T)+\big(1-\varepsilon(\nu)\big)L_{\mathrm{d}}(\nu). \qquad (2)$$

In this approximation, two steps were used for atmospheric compensation and a third step performed temperature-emissivity separation: the first step accounted for sharp featured signal from the sky radiance and the second step accounted for a broad-featured signal that spatially correlated with the sharp-featured signal. The sharper features are usually associated with small gas-phase molecules such as water; the second step accounts for broader features associated with species such as ozone.

For the first step, it is noted that at terrestrial temperatures $B(\nu,T)$ is a smooth function in the longwave infrared, and for many materials observed in the natural environment the term $\varepsilon(\nu)B(\nu,T)$ is often a rather featureless graybody spectrum. Notable exceptions to this generalization are solid materials with reststrahlen features which have large k values, k being the imaginary component of the complex refractive index. Such reststrahlen bands are often observed in the spectra of minerals and other species with highly symmetric cations or anions [20][56-65]. In contrast, the reflected downwelling term, $\big(1-\varepsilon(\nu)\big)L_{\mathrm{d}}(\nu)$, tends to include sharp features due to emission from small molecules such as water in the upper atmosphere [66] and slightly broader features due to emission from other molecules such as ozone. In the first step of the atmospheric compensation strategy, the sharp-featured signal, $L_1(\nu)$, is estimated by fitting a smooth curve to the signal $L(\nu)$ to each pixel in the image [67][68] allowing sharp

features to be ignored. This fit was performed using an asymmetric least squares algorithm that iterates the fit and sequentially de-weights signal with positive residuals until convergence. No basis functions were used in the fit. Two model parameters include a penalty on smoothness and a threshold on non-negative residuals. This approach is analogous to fitting smooth spectral baselines [69].

To estimate the broader features in the downwelling radiance term, $L_2(\nu)$, the second step uses an endmember extraction methodology (a.k.a., multivariate curve resolution [70][71]) applied to the corrected image from the first step given by $L(\nu) - L_1(\nu)$. Endmember extraction is a non-negative matrix factorization (a.k.a., positive matrix factorization) based on the linear mixture model (LMM). For a given pixel, the LMM is given by

$$L(\nu) - L_1(\nu) = \mathbf{Sc} + \mathbf{e} \qquad (3)$$

where $\mathbf{S}$ is a $N \times K$ set of endmembers with N spectral bands and K endmembers and $\mathbf{c}$ is a $K \times 1$ set of pixel-specific contributions. The model fit residuals are given by $\mathbf{e}$. There are many methods for performing endmember extraction. [Please see references 61 and 62 for reviews of many methods and applications.] One of the more popular end-member extraction methods used by spectroscopists is an alternating least-squares (ALS) minimization with non-negativity constraints. The ALS algorithm was used in this work because it is also easy to employ equality constraints (this is an advantage of the ALS algorithm). Other constraints such as smoothness are often employed but were not used in this study. Constraints were used so that the set of endmembers were arranged as

$$\mathbf{S} = [\mathbf{L}_2 \quad \mathbf{b}_1 \quad \mathbf{b}_2 \quad \mathbf{S}_{4-K}] \qquad (4)$$

where the first endmember corresponded to $L_2(\nu)$, the second and third corresponded to blackbody-like signal and the remaining $4 - K$ endmembers were included to span a significant amount of remaining systematic signal in each image. The purpose of $\mathbf{S}_{4-K}$ was to span remaining systematic variance in the data. No additional analysis of $\mathbf{S}_{4-K}$ was performed. To obtain an estimate of $L_2(\nu)$ consistent with the previous and more easily obtained estimate of $L_1(\nu)$, the contributions of the first endmember, $\mathbf{L}_2$, were constrained to match the contributions of sharp featured signal in $L_1(\nu)$, i.e. the spatial statistics for $L_2(\nu)$ match the spatial statistics for $L_1(\nu)$. The $L_1(\nu)$ signal across the images was examined with PCA, and for this work, only 50% of pixels with the highest $L_1(\nu)$ signal were used for equality constraints on $L_2(\nu)$. The second and third endmember spectra, $\mathbf{b}_1$ and $\mathbf{b}_2$, were spectrally equality constrained to Planck functions $B(\nu, 250K)$ and $B(\nu, 350K)$ respectively. The information on $\mathbf{b}_1$ and $\mathbf{b}_2$, was not used further in the present work but are anticipated to be used as a diagnostic in future implementations. Other than non-negativity, $\mathbf{S}_{4-K}$ was not further constrained. The number of endmembers used in the linear mixture model was fourteen ($K = 14$) which was estimated by inspecting a typical image in this study with PCA, so as to provide a reasonable set of basis vectors. This helped avoid adding more noise to the estimate, which can occur if too many endmembers are used, and helped avoid adding a bias to the estimation of $L_2(\nu)$ which can occur if too few endmembers are used. This number could also be based on capture of variance criterion within the $L(\nu) - L_1(\nu)$ image (e.g., 95 to 99%). Comparisons of $\big(1 - \varepsilon(\nu)\big)L_\mathrm{d}(\nu) = L_1(\nu) + L_2(\nu)$ on the aluminum board where $\varepsilon(\nu)$ is very close to zero and $L(\nu) \approx L_\mathrm{d}(\nu)$ shows that $L_\mathrm{d}(\nu) \approx L_1(\nu) + L_2(\nu)$ and that the recovered reflectance of the aluminum is very close to one. This work provides a proof-of-principle, and additional work with other well-characterized scenarios is continuing. The modulated downwelling radiance term is thus approximated as $\big(1 - \varepsilon(\nu)\big)L_\mathrm{d}(\nu) = L_1(\nu) + L_2(\nu)$. The atmospherically corrected image, $L_3(\nu)$, is then simplified to:

$$L_3(\nu) = L(\nu) - L_1(\nu) - L_2(\nu) \approx \varepsilon(\nu)B(\nu, T). \qquad (5)$$

The procedure outlined above provides a first order approximation for atmospheric compensation whose advantages include: 1) $L_d(\nu)$ need not be modeled *a priori*, 2) the algorithm can be automated and applied to entire images without predetermined regions of interest for study, 3) the $L_1(\nu)$, $L_2(\nu)$ and $\big(1-\varepsilon(\nu)\big)L_{\mathrm{d}}(\nu)$ terms are estimated for each pixel individually, and 4) the algorithm is reasonably fast. (The algorithm took 0.5-0.9 minutes per image on a 2017 3GHz iMac processor for images with 320 by 200 pixels and 122 spectral bins.) The procedure allows $L_d(\nu)$ to vary across an image if applicable (e.g., due to shading, variable clouds and sky radiance, and changes in viewing angle across an image).

After atmospheric compensation, the term $L_3(\nu)$ approximates $\varepsilon(\nu)B(\nu,T)$ in each pixel and the maximum brightness temperature in the image, T_{b}, is calculated. The emissivity is estimated as

$$\varepsilon(\nu) = L_3(\nu)/B(\nu,T_{\mathrm{b}}). \qquad (6)$$

and the reflectivity, $R(\nu)$, is calculated as $R(\nu) = 1-\varepsilon(\nu)$. Although T_{b} may not be appropriate for all pixels in the scene, using this high value ensures that $\varepsilon(\nu) \leq 1$ for all pixels and can be refined in subsequent analysis. This assumption of T_{b} does assume one band within one pixel of the image has an emissivity value of 1 but avoids making a similar assumption for every pixel. The image corresponding to $R(\nu)$, $\mathbf{R}$, is passed to the target detection algorithm described in the next section. Although the profile of the emissivity spectrum may be representative of the ground truth, it is recognized that the present estimate given in Equation 6 is subject to a multiplicative ambiguity. This ambiguity occurs because, in the wavenumber range of interest, the Planck function is a smooth sloping curve such that $B(\nu,T) \approx \alpha B(\nu,T_{\mathrm{b}})$ for a non-zero scalar α where $\varepsilon(\nu)B(\nu,T_{\mathrm{b}}) \approx [\varepsilon(\nu)\alpha^{-1}][\alpha B(\nu,T_{\mathrm{b}})]$. The multiplicative ambiguity translates into an offset ambiguity for reflectance. Further information on how estimation errors can affect the final emissivity calculations for various TES approaches can be found in [11][34].

B. Target Detection

The iterative target detection algorithm uses extended and generalized least squares (ELS-GLS) in an iterative methodology in three main steps: Step 1 initializes parameters such as detection thresholds and convergence parameters. Step 2 iteratively classifies the image into clutter and non-clutter. Non-clutter includes potential detections and "no-calls". No-calls are outliers that are unusual with respect to both the clutter and the target. Potential detections are identified at a low detection threshold and identify pixels that potentially contain target signal but should not be included in the clutter model. In Step 3 the potential detections are classified into either true detections (those above a high threshold) or possible detections (those that are higher than the low threshold but lower than the high threshold).

To be specific, the iterative algorithm thus classifies pixels into four classes: detected target signal, possible detections, clutter signal, and no-calls. Before detailing the iterative algorithm, the detector model is first described. For an $M \times N$ image, $\mathbf{R}$, and a single $N \times 1$ target spectrum, $\mathbf{s}$, the ELS-GLS estimator is given by:

$$[\hat{\mathbf{c}} \quad \widehat{\mathbf{T}}] = \mathbf{R}\mathbf{W}^{-1}[\mathbf{s} \quad \mathbf{P}]([\mathbf{s} \quad \mathbf{P}]^{\mathrm{T}}\mathbf{W}^{-1}[\mathbf{s} \quad \mathbf{P}])^{-1}, \quad (7)$$

where $\hat{\mathbf{c}}$ corresponds to the estimated target contribution to each pixel estimated using a non-negativity constraint and $\widehat{\mathbf{T}}$ are estimated coefficients for $\mathbf{P}$. The weight matrix is $\mathbf{W} = \frac{1}{M_{\mathrm{c}}-K}\mathbf{E}_{\mathrm{c}}^{\mathrm{T}}\mathbf{E}_{\mathrm{c}}$ and its inverse is obtained using a regularization procedure outlined in [39] and [40]. For a matrix of clutter spectra, $\mathbf{R}_{\mathrm{c}}$, the columns of $\mathbf{P}$ correspond to basis vectors that span large sources

of variance in $\mathbf{R}_c$ obtained using principal components analysis [35][36]:

$$\mathbf{R}_c = \mathbf{T}_c\mathbf{P}^T + \mathbf{E}_c, \quad (8)$$

where $\mathbf{R}_c$ and $\mathbf{E}_c$ are $M_c \times N$ ($M_c \leq M$), $\mathbf{T}_c$ is a $M_c \times K$ matrix with orthogonal columns and $\mathbf{P}$ is a $N \times K$ matrix with orthonormal columns, whereby $\mathbf{E}_c$ are the residuals of a PCA model of the clutter defined in Equation 6, M_c is the number of clutter pixels and K is the number of principal components in the PCA model. The number of principal components (PCs), K, is typically selected to capture the major variance in $\mathbf{R}_c$ where often $K \ll N$. For the ELS-GLS model, the first PC corresponds to a representative clutter spectrum that, for non-centered data, closely approximates the mean of $\mathbf{R}_c$ [72]. The weighting, $\mathbf{W}^{-1}$, effectively suppresses clutter signal but too strong of a regularization reduces the net analyte signal of the target and lowers sensitivity. In contrast, too weak of a regularization diminishes the specificity (causes too many false alarms). To optimize detection, each clutter scenario considers this tradeoff to provide the desired sensitivity and selectivity. The detection threshold for $\hat{\mathbf{c}}$ is approximated as

$$\hat{c}_{\text{lim}} = t_{\alpha,M_c-K-1}(\mathbf{s}^T\mathbf{W}^{-1}\mathbf{s})^{\frac{-1}{2}}, t_{\text{stat}} = \hat{c}/\hat{c}_{\text{lim}} \quad (9)$$

where t_{α,M_c} is the approximate confidence limit for a t-distribution at the $1-\alpha$ percentile and $M_c - K - 1$ degrees of freedom, and $(\mathbf{s}^T\mathbf{W}^{-1}\mathbf{s})^{\frac{-1}{2}}$ is the estimation error. The t-statistic, t_{stat}, is a ratio of the target contribution to the desired detection threshold displayed in the images below.

The weighted model residuals from (6) are collected in $\hat{\mathbf{E}}$:

$$\hat{\mathbf{E}} = (\mathbf{R} - [\hat{\mathbf{c}} \quad \hat{\mathbf{T}}][\mathbf{s} \quad \mathbf{P}]^T)\mathbf{W}^{-1/2}. \quad (10)$$

The residual vector for the m^{th} row of $\hat{\mathbf{E}}$ is $\hat{\mathbf{e}}_m^T$ for $m = 1, \ldots, M$ and the corresponding weighted Q-residual is the sum-of-squares given by

$$q_m = \hat{\mathbf{e}}_m^T\mathbf{W}^{-1}\hat{\mathbf{e}}_m. \quad (11)$$

A statistical limit for the Q-residual at the $1-\alpha$ percentile, q_α, can be estimated using the method proposed by Jackson and Mudholkar [73][74]. Pixels with $q_m > q_\alpha$ are classified as "no-calls" and are considered anomalous pixels that should not be considered detections and are removed from $\mathbf{R}_c$ during the iterative process.

A challenge for clutter suppression is to identify a set of representative target-free pixels $\mathbf{R}_c$ that can be used for characterizing the clutter covariance but at the same time recognizing that the presence of the target signal in the clutter covariance desensitizes the target detection model [40]. In the iterative approach, the initial approximation for the clutter matrix, $\mathbf{R}_{c,0}$, included all pixels in the image: this is a reasonable assumption for cases where the overall magnitude of signal attributable to target is minor relative to clutter signal as was the case for the images considered in this work.

The iterative target detection algorithm is split into three steps: The first step initializes the clutter matrix $\mathbf{R}_{c,0}$, and three detection thresholds. The first threshold, $\hat{c}_{\text{lim,low}}$, provides a limit for potential detections that should not be included in $\mathbf{R}_c$, and the second, $\hat{c}_{\text{lim,high}}$, is used to determine "true" detections with a high confidence. The third threshold, q_α, determines the sensitivity to

anomalous signal. The objective of Step 2 is to iteratively improve the sensitivity of the target detector algorithm. The second step of the algorithm iteratively identifies potential detections and anomalous pixels based on $\hat{c}_{\mathrm{lim,low}}$ and q_α that are both classified as non-clutter pixels that are iteratively removed from $\mathbf{R}_\mathrm{c}$. The remainder of the pixels in $\mathbf{R}_\mathrm{c}$ are used as clutter pixels in the next iteration. After iteration converges, the pixels included in $\mathbf{R}_\mathrm{c}$ are classified as "clutter signal" and anomalous pixels are classified as "no-calls." The remaining N_{detect} pixels are considered potential detections classified as "detected target signal." In Step 3, the detected target signal class is split into "true detections" based on $\hat{c}_{\mathrm{lim,high}}$ with the remainder of the potential detections classified as "near detections". The spectra in **R** and the target spectrum, **s**, are normalized using a one-norm normalization [40]. Examples using the ELS-GLS target detection algorithm are shown in Section IV.

III. Experimental Methods

Infrard reference spectra and other specifics of the minerals and chemicals used and reported in the dendrograms of Fig. 5 have been detailed previously [20][55].

A. Sample Preparation and Laboratory Hemispherical Reflectance (HRF) Measurements.

Twenty-four samples were prepared mostly as powders in Nalgene® cup lids, with five samples in solid form affixed to the boards as polished minerals/rocks, the remaining 19 samples being the powdered minerals and chemicals. Pure chemicals were obtained from Aldrich and minerals were obtained from other commercial sources, as has been detailed in [20]. Both hemispherical reflectance (HRF) and diffuse-only reflectance (DRF) spectra were measured in the laboratory and the HRF were utilized as the target spectra (endmembers) for this study. The broadband laboratory reference spectra were collected from 1.33 to 16.6 μm (7500 to 600 cm^{-1}) at 2.0 cm^{-1} resolution, typically averaging 2048 interferogram scans. Details of the laboratory parameters and settings can be found elsewhere [20][53].

B. Field Measurements

For field measurements, both the hard minerals and the powdered samples (in Nalgene cups) were affixed to a plywood board which was tilted at a 45° angle relative to ground. One board had the raw plywood as background and the other was covered with aluminum foil. Samples were placed in a grid manner of four rows and six columns, with 8 inches between columns and 11.3 inches between rows [20]. Forty images of the samples were collected on 4 October 2017, ranging from 11:20 to 21:32 local time using the Telops Hyper-Cam, an LWIR hyperspectral imager on the Pacific Northwest National Laboratory (PNNL) campus (46.319°N, 119.283°W). Field measurements were in the range of 1300-850 cm^{-1} (7.7 - 11.7 μm) at a resolution of 3 cm^{-1}. Further experimental settings are found elsewhere [20]. As shown in the dendrogram of Figure 5 and discussed below, many of the targets have similar signatures that can easily result in false alarms for target detection algorithms. Examples analyses using the ELS-GLS and ACE target detection algorithm are shown in Section IV.

C. Software

Computations were performed using MATLAB 2022,23b and 24a [75] and PLS_Toolbox with MIA_Toolbox (multivariate image analysis) [76].

IV. Results

Atmospheric compensation was performed for each image individually, and target detection algorithms were executed on each of the compounds for each of the forty images, i.e. both for the aluminum background and the plywood background. Identical target detection meta-parameters were used for all images.

A. Atmospheric Compensation

As an example, the top row of Fig. 3 and 4 show the measured radiance on an aluminum board designated as C1B1 for four selected minerals corresponding to the laboratory reflectance spectra plotted in Fig. 1. The example pixel spectra shown in Fig. 3 and 4 are from ground truth ROI determined by visual inspection and provide an illustration of the natural variability in the measured radiance from a reasonably uniform material. Note, however, manual delineation of a ROI is not needed for the automated approach. The bottom panels of Fig. 3 and 4 plot the estimated reflectance for the same selected pixels after atmospheric compensation and temperature-emissivity separation. For comparison, each plot includes the corresponding laboratory measured reflectance spectrum (also plotted in Fig. 1). The measured radiance for onyx-calcite in the top row (2nd panel) shows water and ozone features from the reflected downwelling radiance, $L_{\mathrm{d}}(\nu)$. These features have been successfully accounted for using atmospheric compensation and are not present in the estimated reflectance for onyx-calcite in the bottom panel. In general, the spectral profiles of the estimated reflectance are quite similar to the corresponding library spectra with identical peak positions nearly all features. The estimated reflectance spectral bands (lower frames, topmost traces) are more compressed, however, with features displaying reduced amplitudes vs. the corresponding library spectra. For example, the estimated reflectance spectral shape for muscovite is notably flatter than the corresponding library spectrum but does have a very similar overall spectral profile. The flatness of the estimated reflectance may be due, in part, to the Level 2 (L_2) compensation that accounts for downwelling radiance from ozone. The ozone signal is present near the 9.6 μm (1040 cm^{-1}) band from muscovite and may thus interfere with the atmospheric compensation. We note that there is also a gradual increase in the baseline towards shorter wavelengths (increased wavenumbers), likely due to the (1/λ) spectral dependence of some phenomenon such as i) a scattering mechanism such as Mie scattering arising from particles of a size comparable to the light wavelength, ii) some blurring from neighboring pixels, or iii) an offset in the temperature emissivity algorithm caused by the selection of temperature. Further analysis is needed to better understand the phenomenon.

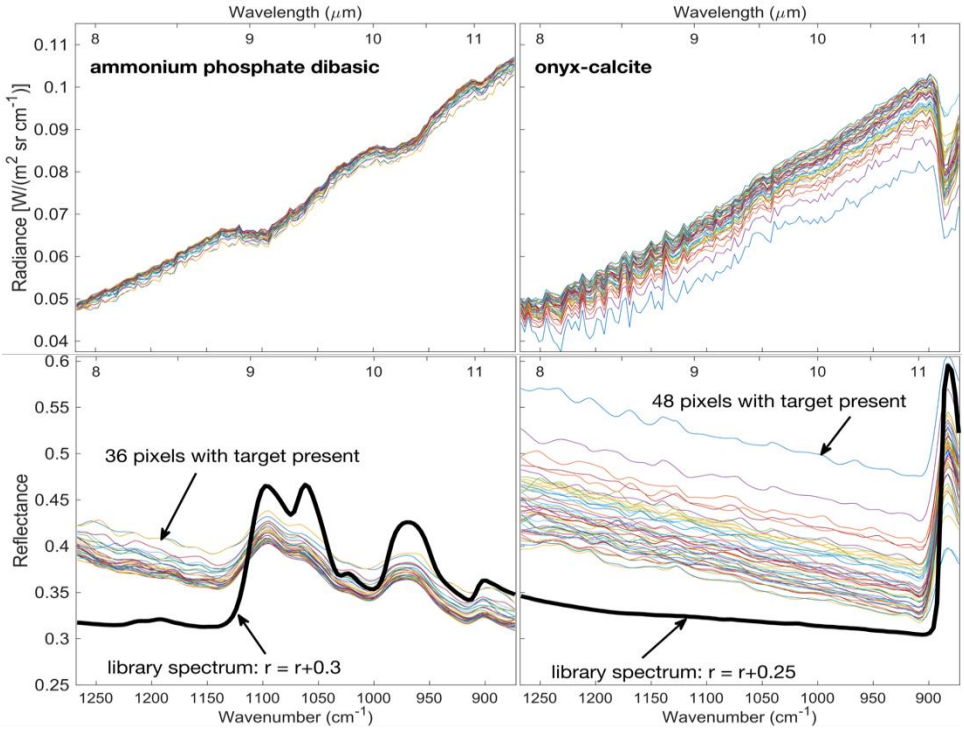

Fig. 3. Top row plots the measured radiance for two example minerals ammonium phosphate dibasic and onyx-calcite on aluminum board C1B1. The bottom frames plot the corresponding reflectance after atmospheric compensation and temperature emissivity separation, with the quantitative library spectra plotted in units of reflectance ($0 \leq R(\nu) \leq 1$).

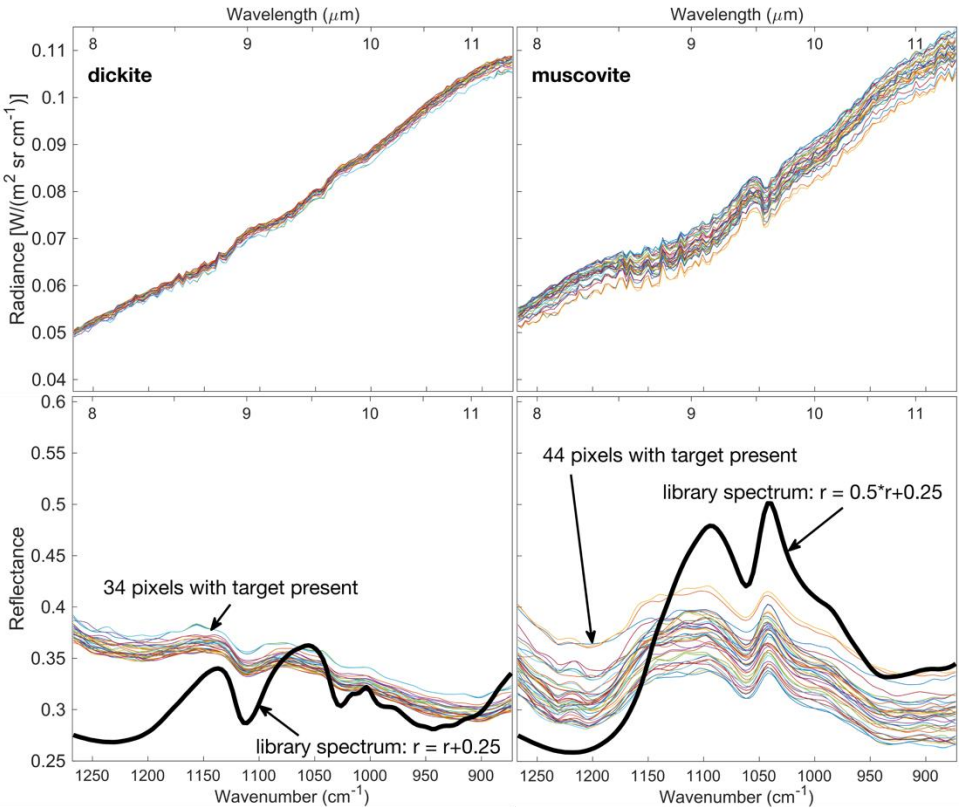

Fig. 4. Top row plots the measured radiance for two example minerals dickite and muscovite on aluminum board C1B1. The bottom frames plot the corresponding reflectance after atmospheric compensation and temperature emissivity separation, with the quantitative library spectra in units of reflectance ($0 \leq R(\nu) \leq 1$).

B. Target Detection

Twenty-two reflectance spectra were examined in this study (corresponding to the twenty minerals on the board plus a spectrum of a mineral not on the board and the spectrum of Nalgene) and example results are shown in Fig. 3 and 4 for ammonium phosphate dibasic [$(NH_4)_2HPO_4$], onyx calcite, dickite and muscovite. Cluster analysis was used to gain insight for differences in target detection performance as a starting place, as it was expected that minerals in the same cluster would share similar performance. Furthermore, as the target detection had false alarms, it was common, but not always the case, that the false alarm would be from a mineral in the same cluster. Fig. 5 (left) shows a K-means cluster analysis dendrogram of the minerals examined in the study. For the cluster analysis, the laboratory measured reflectance spectra, R, were augmented in the spectral mode with the second derivative spectra, $\mathrm{d}R$ to emphasize spectral shape differences in the distance calculations for K-means. A Savitzky-Golay smooth with a seven-point window, second order fit and second order derivative was used to estimate $\mathrm{d}R$ [77]. For visualization, the minerals in a mineral cluster were assigned the same color, and the same color scheme was used for Fig. 5 (right) which plots the reflectance spectra for the twenty-two minerals. Observations for each cluster based on Fig. 5 and examining detection images are provided below. Example detection images are given in Figs. 6 and 7 for ammonium phosphate dibasic and dickite.

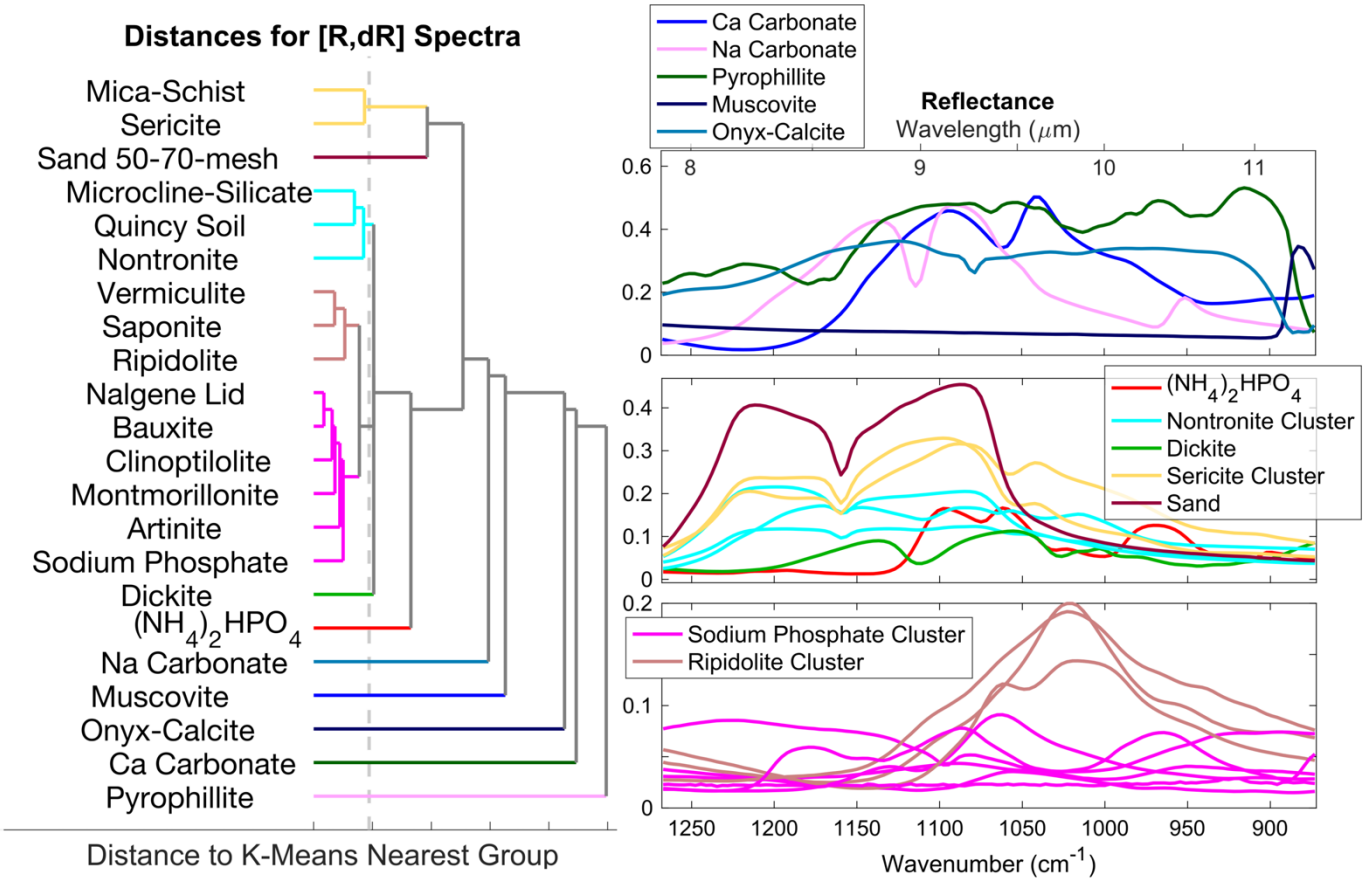

Fig. 5. (left) K-Means clustering dendrogram of mineral reflectance included in the study. (right) Corresponding reflectance spectra colored using the dendrogram clusters, where spectra of same color are from same cluster with a single mineral called out as label.

The hyperspectral images of the boards were recorded over the course of the day, which corresponds to changing temperatures and changing solar angles over the course of the measurements. On 4 October 2017, the sunrise was at 7:00, solar noon was 12:45, and sunset was at 18:31 local time [78]. Temperature increased throughout the day with a maximum in late afternoon [79]. The last four images were acquired after sunset. Although several combinations were examined, the algorithm parameters were identical for all images: $\hat{c}_{\mathrm{lim,low}}$ the confidence limit was 80% ($t_{0.8,M_c-K-1}$), $\hat{c}_{\mathrm{lim,high}}$ the confidence limit was 90% ($t_{0.9,M_c-K-1}$), and for q_α the limit was set at 99.999%, number of ELS principal components = 3, and GLS regularization maximum condition number = 10. The parameters were not optimized for any specific-image and the performance discussed below represents the performance that might be expected from a large-scale screening of multiple images. It is important to note that excluding pixels with high residuals on the target detection models reduced the number of false alarms significantly for all materials studied. These pixels are considered "no-calls" and appear as black pixels in Figs. 6 and 7.

The sodium phosphate cluster corresponds to a group of materials that were difficult to detect and classify due to their low reflectance ($R < 0.1$) and relatively featureless spectra. As expected, these minerals tended to not be detected or have excessive false alarms for the plywood boards. Bauxite, clinoptilolite, and montmorillonite showed weak detections on plywood but also included several false alarms. In contrast, sodium phosphate (also in this cluster) was detected in all plywood images, with the algorithm exhibiting only a small number of false alarms on pyrophyllite. The t-statistic for the sodium phosphate detections increased as time of day increased, and was highest at 19:54 local time.

Target detection algorithm performance for minerals in the ripidolite cluster was better than those in the sodium phosphate cluster. These minerals were weakly detected on aluminum but more strongly detected on plywood, with the algorithm exhibiting false alarms only on other members of the same cluster. Target detection with targets of ripidolite and vermiculite had similar detection performance, but there were unexpected false alarms for mica-schist as the target on the plywood board. Target detection scores (with saponite as the target) were similar to scores with ripidolite as the target and vermiculite as the target, but target detection with saponite as the target had a greater number of false alarms on plywood. It is not surprising that ripidolite, vermiculite, and saponite were each falsely reported as the others in the target detection algorithm, given the similarity of their spectra as seen in Fig. 5, brown traces.

For the nontronite cluster on the aluminum board, no target detections were observed for microline-silica or Quincy soil, while nontronite itself afforded only weak detections. The algorithm detected all three minerals on plywood, with the algorithm having excessive false alarms both on the boards and on the background for both targets of microline-silicate and Quincy soil. It is noted that all three of these minerals had strong detection scores as sand for plywood: This is not surprising because sand has a higher reflectance and a similar spectral shape to microline-silicate, Quincy soil, and nontronite [Fig. 5 left] as all are dominated by the Si-O reststrahlen doublet feature near 8.6 μm (1160 cm^{-1}) [20]. Both sericite and mica-schist were detected on aluminum and plywood, but higher confidence detections were reported on plywood. Both mineral targets had the algorithm give false alarms on sand likely due to sand having a higher reflectance and a similar spectral shape to sericite and mica-schist [Fig. 5 (left)]. Algorithm false alarms for targets on plywood increased toward the end of the diurnal cycle (evening) indicating the importance of the infrared reflected light term in (1). The algorithm detected sand on aluminum but with weak false alarms on both nontronite and sericite samples. Sand was also detected on plywood with strong false alarms on the nontronite and sericite samples.

The dendrogram of Fig. 5 (left) shows that pyrophyllite has strong reflectance and the most unique spectrum of the minerals under study (Fig. 5 right). Pyrophillite was detected on the aluminum boards with no false alarms. Pyrophillite was also detected on plywood, albeit with increased false alarm rates. Some false negatives were observed for pyrophyllite, however. In contrast, sodium carbonate was not detected on the aluminum board. This was somewhat surprising given that sodium carbonate has a greater overall reflectance and a moderately unique reflectance spectrum with a band edge near 11.1 μm (900 cm^{-1}) (Fig. 5). But it is possible that the non-detection was due to the relatively flat spectral shape for sodium carbonate. Weak detections for sodium carbonate were also observed on plywood. Calcium carbonate has a strong reflectance and a more unique spectrum (Fig. 5) and was detected on both aluminum and plywood as a pure chemical and in a 50:50 mixture of sand and calcium carbonate. No false alarms were observed on aluminum, but a few false alarms were detected on plywood.

Detection images are shown in Figs. 6 and 7 for $(NH_4)_2HPO_4$ and dickite, respectively, where yellow coloring indicates target detections, black are no-calls, and dark blue are clutter. The images are saturated to lie on $1 \leq \mathrm{t-statistic} \leq 2$ based on the $c_{\mathrm{lim,high}}$. Fig. 5 shows that $(NH_4)_2HPO_4$ has a unique spectrum but a low reflectance. Fig. 6 (left) shows that $(NH_4)_2HPO_4$, was weakly detected on aluminum background board C1B1 with no false alarms. It is also noted that the target detection scores were weakest for the last board measured at time 21:32 after the sun had set. Fig. 6 (right) shows that $(NH_4)_2HPO_4$, was easily detected on plywood board designated C1B3 but also had some weak false alarms attributed to the low reflectance for $(NH_4)_2HPO_4$.

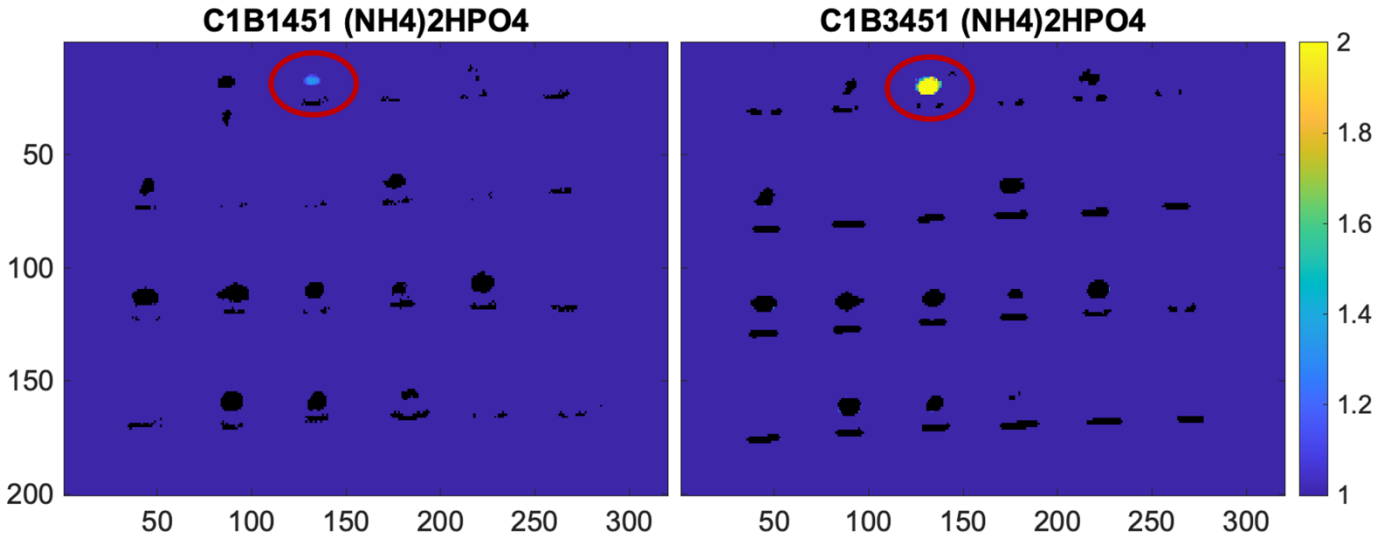

Fig. 6. Target detection t-statistic for ammonium phosphate dibasic. (left) Results for aluminum board C1B1 and(right) plywood board C1B3. Ground truth location for $[(NH_4)_2HPO_4]$ is indicated by a red circle. No-calls are black pixels.

Figure 7 shows that dickite has low reflectivity and a relatively flat spectrum but is unique from the sodium phosphate cluster. Fig. 7 (left) shows that dickite was not detected on aluminum board C1B1. However, the target detection algorithm detected dickite on plywood board C1B3 (Fig. 7 right) and had weak false alarms for the montmorillonite sample below dickite, likely due to the common broad band at 9.4 μm (1060 cm^{-1}) for the two minerals.

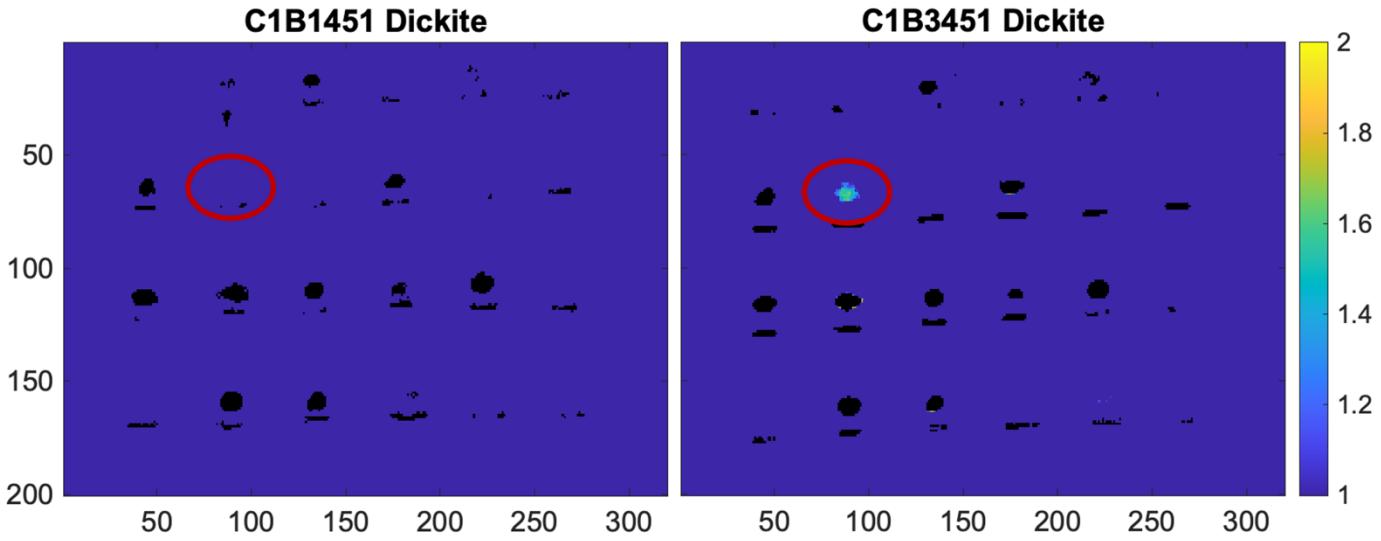

Fig. 7. Target detection t-statistic for dickite. (left) Results for aluminum board C1B1 and(right) plywood board C1B3. Ground truth location for dickite is indicated by a red circle. No-calls are black pixels.

To provide a comparison, the adaptive cosine estimator (ACE) target detector was applied to the atmospherically compensated scenes for the estimated reflectance spectra in the image. Briefly, for the m^{th} pixel, $\mathbf{r}_m$, in the image, the centered and whitened response, $\tilde{\mathbf{r}}_m$, is

$$\tilde{\mathbf{r}}_m = \mathbf{W}_c^{-1/2}(\mathbf{r}_m - \bar{\mathbf{r}}_c) \qquad (12)$$

where $\bar{\mathbf{r}}_c$ is the mean of the clutter spectra, $\mathbf{R}_c$, identified by the iterative target detection algorithm, and the clutter covariance, $\mathbf{W}_c$, is given by

$$\mathbf{W}_c = \frac{1}{M_c - 1}(\mathbf{R}_c - \mathbf{1}\bar{\mathbf{r}}_c^T)(\mathbf{R}_c - \mathbf{1}\bar{\mathbf{r}}_c^T) \qquad (13)$$

where $\mathbf{1}$ is a $M_c \times 1$ vector of ones. The centered and whitened target is

$$\tilde{\mathbf{s}}_m = \mathbf{W}_c^{-1/2}(\mathbf{s}_m - \bar{\mathbf{r}}_c) \qquad (14)$$

and the ACE detector is given by

$$y_{\mathrm{ACE},m} = \frac{\tilde{\mathbf{r}}_m^T}{|\tilde{\mathbf{r}}_m|_2}\frac{\tilde{\mathbf{s}}_m^T}{|\tilde{\mathbf{s}}_m|_2} \qquad (15)$$

where $|\tilde{\mathbf{r}}_m|_2 = (\tilde{\mathbf{r}}_m^T\tilde{\mathbf{r}}_m)^{-1/2}$ is the two-norm and $-1 \leq y_{\mathrm{ACE},m} \leq 1$. A comparison of the target detection approach outlined in this paper and with ACE can be seen in Fig. 8. The left of Fig. 8 is the target detection approach of this paper (matches right of Fig. 6), and the right of Fig. 8 is the ACE target detection approach.

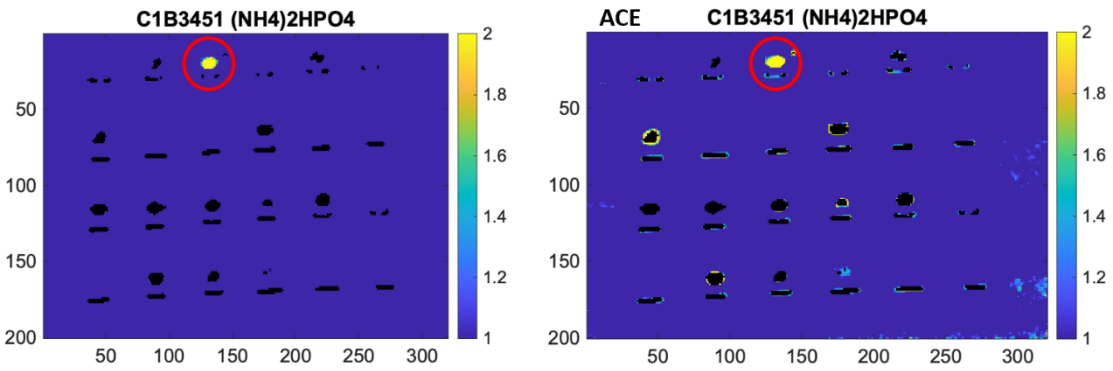

Fig. 8. Target detection for ammonium phosphate dibasic on plywood board C1B3. Left is the target detection approach from this paper (from right frame of Fig 6). Right frame is for the ACE target detector. Ground truth is indicated by a red circle. No-calls are black pixels.

As can be seen in Fig. 8, both algorithms successfully detected $(NH_4)_2HPO_4$, but the ACE target detection algorithm displayed an increased number of false alarms on the plywood board for ammonium phosphate dibasic and it is noteworthy that ACE showed false alarms on pixels in the background behind the plywood board. These images use the same detection threshold in both algorithms as well as the same atmospheric compensation, so as to compare, as close possible, the two algorithms for target detection. Both analyses used the same clutter; without this clutter the ACE target detection displayed still additional false alarms to those shown in Fig. 8. A user can adjust thresholds post processing to determine which threshold setting provides the desired results and likely with additional tweaking the ACE detector would have less false alarms. On some of the boards and images, ACE performed comparably, but, in general, when they differed in performance the ACE algorithm displayed successful detection but an increased number of false alarms.

For comparison, Fig. 9 (left frame) shows receiver operator characteristic (ROC) curves for iterative target detection and ACE with an ammonium phosphate dibasic $(NH_3)_2PO_4$ target on the C1B3 plywood board corresponding to Figure 8. The curves were calculated for true negative pixels and pixels fully filled with target. Mixed pixels were not included in the calculation. The ROC curves show that both target detection and ACE have a detection threshold that perfectly detects full target pixels from true negative pixels, however it is noted that in an automated analysis with unknown ground truth a detection threshold also needs to be established automatically from the image under analysis. Figure 9 (right frame) elaborates on the ROC curves to show detection performance versus the corresponding detection statistic: the cosine for ACE and the t-statistic for target detection. The vertical red line indicates the 95% false alarm threshold calculated from the null (clutter) distributions used for Fig. 8. It is noted that the same clutter, $\mathbf{R}_c$, that had no-calls excluded was use for target detection and ACE although in practice ACE does not typically identify no-calls.

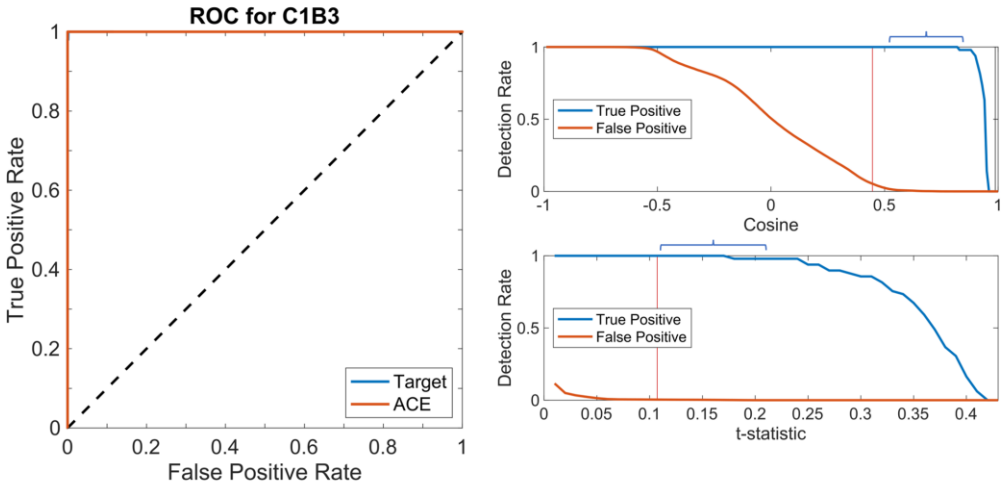

Fig. 9. (left) ROC curves for iterative target detection and ACE. (right) Detection performance versus the corresponding detection statistic: the cosine for ACE and the t-statistic for target detection. The approximate region of split between true negatives and full target pixels is indicated.

Fig. 10 shows the estimation error $[(\mathbf{s}^T\mathbf{W}^{-1}\mathbf{s})^{\frac{-1}{2}}]$ for the four example minerals on all ten boards studied. The estimation error was used with the confidence limit, $c_{\text{lim,high}}$, to calculate the t-statistic. The top row of Fig. 10 corresponds to the aluminum boards and the bottom row to the plywood boards. Each set of five bars correspond the time of image acquisition from left to right for the five bars in each group. The greater the error, the more similarly the spectrum maps to the background clutter.

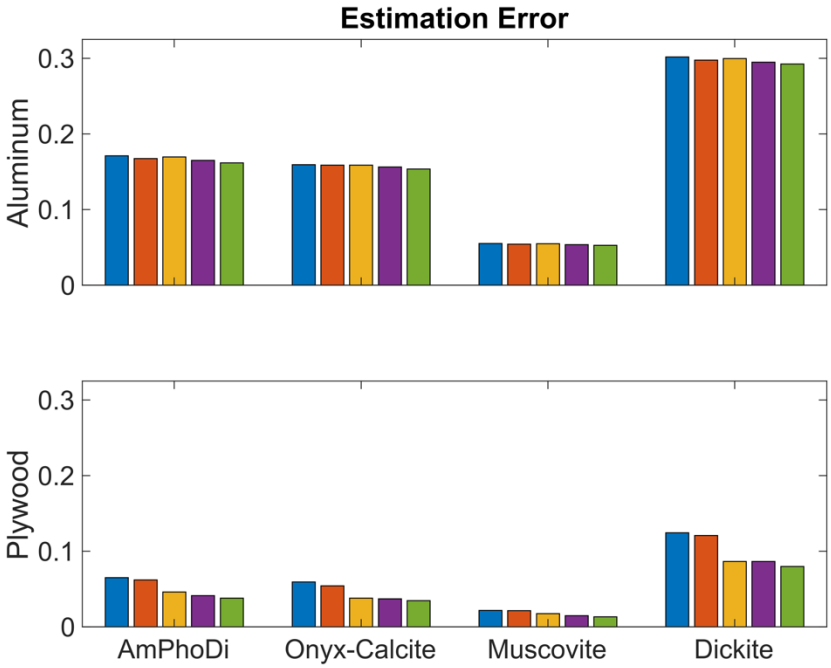

Fig. 10. Estimation error for aluminum board (top) and plywood board (bottom). Each set of fives bars correspond the time of image acquisition from left to right. AmPhoDi is ammonium phosphate dibasic.

The plots in Fig. 10 are consistent with the observations given above for each of the 22 minerals. In general, the target detection estimation error was higher on the aluminum boards (Fig. 10 top panel) compared to the plywood boards. Detection algorithm performance for dickite was poor and had the highest estimation error of the four example minerals, due largely to it weak-featured spectrum in the LWIR. In contrast, ammonium phosphate dibasic exhibited better detectivity using this algorithm with a lower estimation error, due to its strong reflectance and structured spectrum as seen in Figure 3 [59]. Muscovite had the lowest target detection estimation error for these samples and highest false alarms on plywood boards.

V. Discussion and Conclusions

Improvements in hyperspectral imaging hardware are resulting in higher resolution in the spatial, spectral, and temporal domains: more data, more quickly. The improvements are generating a corresponding need for algorithms that can efficiently and accurately screen large numbers of HS frames. For standoff applications the following steps are crucial: 1) atmospheric compensation and temperature-emissivity separation, 2) target and anomaly detection with available library spectra, and 3) optimization of algorithm parameters tuned to specific imaged scenarios. This work has shown good progress at implementing Steps 1 and 2 and provided insights expected to aid in Step 3.

The atmospheric compensation algorithm presented in this paper was based on the observation that downwelling atmospheric radiance tends to include sharp spectral features that can be accounted for using an asymmetric least squares baselining algorithm. The approach was relatively fast, used only in-scene information, did not require manual selection of regions of interest, and provided easily interpretable results. For example, additional forensics could be performed on the corrected spectra and the downwelling radiance signal to identify anomalies and pixels that exhibit a blackbody signal. Anomalies often warrant additional

inspection while blackbody pixels would not demonstrate noteworthy emissivity spectra. A simple temperature-emissivity algorithm was employed to the corrected spectra. The resulting estimated reflectance spectra generally had spectral shapes similar to the library spectra but were typically offset. It was noted that the estimated reflectance spectra for a few of the minerals studied (e.g., muscovite) showed a flattening of the spectral shape compared to the library spectra.

Target detection is often employed locally, e.g., with a moving window of pixels, or applied to partitioned images. Typically, detection sensitivity improves for local models because fewer sources of clutter (interference signal) need to be accounted for. Target detection algorithm sensitivity also improves by removing target signal from the clutter model. Moving window approaches often use guard pixels (buffer pixels around the PUT) to avoid including target signal in the pixel under test, but this approach is computationally expensive and slow. In comparison, the algorithm presented in this paper excludes the potential target signal iteratively based on a low detection threshold (in this study two to three iterations were typical) and provides fast screening of the images. The approach did not require manual selection of regions of interest and avoided excessive false alarms by excluding pixels with high residuals in the detection model and classed these pixels as no-calls. Pixels classified as no-calls are considered anomalies relative to the target and typical clutter. To demonstrate the ability to automatically screen images for signals of interest, this study applied iterative target detection to each image without manually selecting regions of interest. The approach is expected to further improve when applied to individual segments of partitioned images but can still be applied to entire images. Improvements are also expected when algorithm parameters are tuned to individual segments in specific imaged scenarios. Next steps also require testing this approach on a larger, more complex field scene with less certainty in the ground truth.

For this study, algorithm parameters for atmospheric compensation and iterative target detection (e.g., detection thresholds and clutter modeling) were held constant. Although some atmospheric effects were observed, differences in detection algorithm performance were then primarily attributed to changes in the target signal (its reflectance spectrum) and sources of clutter in an image. Our findings may be summarized as follows: First, the target detection algorithm was more sensitive (more known target pixels were detected i.e., it had more true positives detected) on the plywood boards compared to the aluminum boards. Second, the number of false alarms was significantly reduced by setting pixels with high residuals on the target detection model as “no-calls”. Third, lower estimation errors tended to result in higher sensitivity. Fourth, the algorithm has poor sensitivity to spectra with low %R and flat (featureless) spectral shapes. Fifth, spectra with high reflectance tended to have high sensitivity. And sixth, as expected, detections on target spectra with unique spectral shapes and sharper features tended to be better with fewer false alarms than other spectra [80][81].

The approach presented in this paper is an efficient first order screening methodology for automated atmospheric compensation and target detection in standoff hyperspectral imaging. Future work could include the use of target mineral spectra, once target minerals have been identified, as the basis vectors. Additionally, and significantly, an automated procedure for identifying scenario-specific algorithm parameters is needed.

DATA SHARING: Data sharing is not applicable to this article, as no new data were created or analyzed.

REFERENCES

[1] Sneha, A. Kaul, “Hyperspectral imaging and target detection algorithms: a review.,” *Multimedia Tools Appl*., vol 81, no. 30, pp. 44141-44206, 2022, doi: 10.1007/s11042-022-13235-x.

[2] Y. Zhang, W. Hua, F. Huang, Q. Wang, and W. Suo, “Research status of hyperspectral anomaly target detection,” *J. Phys. Conf. Ser.*, vol 1325, no. 1, 2019-10, p. 012178, doi: 10.1088/1742-6596/1325/1/012178.

[3] N. M. Nasrabadi, "Hyperspectral Target Detection: An Overview of Current and Future Challenges," *IEEE Signal Process Mag.*, vol. 31, no. 1, pp. 34-44, 2013, doi: 10.1109/MSP.2013.2278992.

[4] S. Matteoli, M. Diani, and G. Corsini, "A tutorial overview of anomaly detection in hyperspectral images," *IEEE Aerosp. Electron. Syst. Mag.*, vol. 25, no. 7, pp. 5–27, 2010, doi: 10.1109/MAES.2010.5546306.

[5] C. E. Caefer, M. S. Stefanou, E. D. Nielsen, A. P. Rizzuto, O. Raviv, and S. R. Rotman, "Analysis of false alarm distributions in the development and evaluation of hyperspectral point target detection algorithms," *Opt. Eng.*, vol. 46, no. 7, pp. 076402-076415, 2007, doi: 10.1117/1.2759894.

[6] D. Manolakis, D. Marden, and G. A. Shaw, "Hyperspectral Image Processing for Automatic Target Detection Applications," *Lincoln Laboratory Journal*, vol. 14, no. 1, pp. 79-116, 2003.

[7] N. B. Gallagher, "Target detection of melamine in wheat gluten in a NIR infrared hyperspectral image," *NIR news*, vol. 33, no. 3-4, 2022 doi: 10.1177/09603360221099920.

[8] L. Drumetz, J. Chanussott, and C. Jutten, "Variability of the Endmembers in Spectral Unmixing," in *Hyperspectral Imaging*, 1st Ed, Elsevier, Amsterdam, Netherlands, 2019, vol. 32, pp. 167-203, doi: 10.1016/B978-0-444-63977-6.00009-2.

[9] J. Theiler, A. Ziemann, S. Matteoli, and M. Diani, "Spectral Variability of Remotely Sensed Target Materials: Causes, Models, and Strategies for Mitigation and Robust Exploitation," *IEEE Geosci. Remote Sens. Mag*, vol. 7, no. 2, pp. 8-30, 2019, doi: 10.1109/MGRS.2019.2890997.

[10] T. Burr, B. R. Foy., H. Fry, and B. McVey, "Characterizing clutter in the context of detecting weak gaseous plumes in hyperspectral imagery," *Sensors*, vol. 6, no. 11, pp. 1587-1615, 2006, doi: 10.3390/s6111587.

[11] M. Pieper, D. Manolakis, and E. Truslow *et al.,* "Performance limitations of temperature-emissivity separation techniques in longwave infrared hyperspectral imaging applications", *Optical Engineering*, vol. 56, p. 081804, 2017, doi: 10.1117/1.OE.56.8.081804.

[12] H. F. Grahn and P. Geladi, "Introduction" in *Techniques and Applications of Hyperspectral Image Analysis*, West Sussex, England: John Wiley & Sons, pp. 181-201, 2007.

[13] T. Adao, J. Hruska, L Padua, J. Bessa, E. Peres, and R. Morais *et al.,* "Hyperspectral Imaging: A Review on UAV-Based Sensors, Data Processing and Applications for Agriculture and Forestry," *Remote Sensing*, vol. 9, no. 11, p. 1110, 2017-11, doi:10.3390/rs9111110.

[14] P. Singh, P. C. Pandey, G.P . Petropoulos, A. Pavlides, P. K. Srivastava, and N. Koutsias *et al.,* "Advantages of hyperspectral over multispectral data" in *Hyperspectral Remote Sensing Theory and Applications*, Elsevier, 2020, pp. 121-146, doi: 10.1016/B978-0-08-102894-0.00009-7.

[15] K. Lausten and R. Resmini, "A new approach to infer surface emissivity parameters from longwave infrared hyperspectral measurements", in Proceedings of SPIE, 2006, Vol. 6233, no. 1, pp.62331W-623331W-10

[16] R. DiStasio and R. Resmini, "Atmospheric Compensation of Thermal Infrared Hyperspectral Imagery with the Emissive Empirical Line Method and the In-Scene Atmospheric Compensation Algorithms: A Comparison", in Proceedings of SPIE, 2010, Vol. 7695, No. 1, pp. 76952B-76952B-12

[17] R. Kaiser, D. Vititoe, and A. Andrews, "Detecting Low-Emissivity Objects in LWIR Hyperspectral Data and the Corresponding Impact on Atmospheric Compensation", in Proceedings of SPIE, 2003, vol. 5093, no. 1, pp 705-718

[18] F. Kruse, M. McDowell, and M. Velez-Reyes "Analysis of multispectral and hyperspectral longwave infrared (LWIR) data for geologic mapping", in Proceedings of SPIE, 2015, vol. 9472, Algorithms and Technologies for Multispectral, Hyperspectral, and Ultraspectral Imagery XXI, 94721E, https://doi.org/10.1117/12.2176657

[19] B. Yousefi, C. Castanedo, X. Maldague, and G. Beaudoin, "Assessing the reliability of an automated system for mineral identification using LWIR hyperspectral infrared imagery", Minerals Engineering, 2020, Vol. 155, p. 106409

[20] T. L. Myers, T. J. Johnson, N. B. Gallagher, B. E. Bernacki, T. N. Beiswenger, and J. E. Szecsody *et al.*, "Hyperspectral Imaging of Minerals in the Longwave Infrared: The Use of Laboratory Directional-Hemispherical Reference Measurements for Field Exploration Data," *J. Appl. Remote Sens.*, vol. 13, no. 3, p. 034527, 2019, doi: 10.1117/1.JRS.13.034527.

[21] E. J. Ientilucci, and S. Adler-Golden, "Atmospheric Compensation of Hyperspectral Data," *IEEE Geoscience and Remote Sensing"*, vol. 7, no. 2, pp. 31-50, 2019-06, doi: 10.1109/MGRS.2019.2904706

[22] B. Hapke, "Theory of Reflectance and Emittance Spectroscopy," 2nd ed., New York, NY, USA: Cambridge University Press, 2012, ISBN: 978-0-521-88349-8.

[23] S. Young, B. Johnson, and J. Hackwell, "An in-scene method for atmospheric compensation of thermal hyperspectral data", Journal of Geophysical Research, 2022, Vol. 107

[24] F. Lemaitre, L. Poutier, and Y. Boucher, "Atmospheric correction of airborne infrared hyperspectral images by direct estimation of the radiative terms", IEEE, Workshop on Hyperspectral Image and Signal Processing: Evolution in Remote Sensing, 2010, p.1-4

[25] Spectral Sciences Inc, http://modtran.spectral.com/

[26] M. Nazeer, C. O. Ilori, M. Bilal, J. E. Nichol, W. Wu, and Z. Qiu *et al.,* "Evaluation of atmospheric correction methods for low to high resolutions satellite remote sensing data", *Atmospheric Research"*, vol. 249, p. 105308, 2021, https://doi.org/10.1016/j.atmosres.2020.105308.

[27] T. Cooley, G. P. Anderson, G. W. Felde, M. L. Hoke, A. J. Ratkowski, and J.H. Chetwynd *et al.,* "FLAASH, a MODTRAN4-based Atmospheric Correction Algorithm, Its Application and Validation", *IEEE International Geoscience and Remote Sensing Symposium*, 07 November 2002, doi: 10.1109/IGARSS.2002.1026134.

[28] NV5 User Guide for Atmospheric Corrections with FLAASH, https://www.nv5geospatialsoftware.com/docs/FLAASH.html#Atmoshperic, accessed March 2024.

[29] S. Adler-Golden, P. Conforti, M. Gagnon, P. Tremblay, and M. Chamberland, "Long-wave infrared surface reflectance spectra retrieved from Telops Hyper-Cam imagery," in *Proc. SPIE*, vol. 9088, 2014, doi: 10.1117/12.2050446.

[30] M. Yang, Y. Hu, H. Tian, F. A. Khan, Q. Liu, an J.I. Goes *et al.*, "Atmospheric Correction of Airborne Hyperspectral CASI Data Using Polymer, 6S and FLAASH," *Remote Sensing*, vol. 13, p. 5062, 2021, doi: 10.3390/rs13245062.

[31] W. J. Moses, A. A. Gitelson, R. L. Perk, D. Gurlin, D. C. Rundquist, and B. C. Leavitt *et al.,* "Estimation of chlorophyll-a concentration in turbid productive waters using airborne hyperspectral data," *Water Research*, vol. 46, pp. 993-1004, 2012, doi: 10.1016/j.watres2011.11.068.

[32] P. Mruthyunjaya, A. Shetty, P. Umesh, and C. Gomez, "Impact of Atmospheric Correction Methods Parametrization on Soil Organic Carbon Estimation Based on Hyperion Hyperspectral Data," *Remote Sensing*, vol. 14, p. 5117, 2022, doi: 10.33909/rs14205117.

[33] A. Maher and N. Ghazal, "Removing atmospheric effects for Multi spectral images (OLI 8) using ATCOR model", Materials Science and Engineering, 2020-03, Vol. 757 (1), p.12072

[34] J. Ash and J. Meola, "Temperature-emissivity separation for LWIR sensing using MCMC", in Proceedings of SPIE", 2016, Vol. 9840

[35] B. Bro and A. K. Smilde, "Principal Components Analysis," *Anal. Methods*, vol. 6, pp. 2812-2831, 2014, doi: 10.1039/c3ay41907j.

[36] J. E. Jackson, "A User's Guide to Principal Components," New York, NY, USA: John Wiley & Sons, 1991, ISBN: 0-471-62267-2, doi: 10.2307/2982678.

[37] C. Aitken, "On Least-squares and Linear Combinations of Observations," in *Proceedings of the Royal Society of Edinburg*, vol. 55, pp. 42-48, 1936, doi: 10.1017/S0370164600014346.

[38] G. L. Turin, "An Introduction to Matched Filters," *IEEE Trans. Inf. Theory*, vol. 6, no. 3, pp. 311-329, 1960, doi: 10.1109/TIT.1960.1057571.

[39] T. A. Blake, J. F. Kelly, N. B. Gallagher, P. L. Gassman, and T. J. Johnson, "Passive Detection of Solid Explosives in Mid-IR Hyperspectral Images," *Anal. Bioanal. Chem.*, vol. 395, no. 2, pp. 337-348, 2009, doi: 10.1007/s00216-009-2907-5.

[40] N. B. Gallagher, R. Goyetche, J. M. A. Rubio, and S. Kucheryavskiy, "Extended Least Squares (ELS) and Generalized Least Squares (GLS) for Clutter Suppression in Hyperspectral Imaging: A Theoretical Discussion," *Chemometr. Intell. Lab.*, vol. 244, no. 0, p. 105032, 2024, doi: 10.1016/j.chemolab.2023.105032.

[41] D. Manolakis, M. Pieper, E. Truslow, T. Cooley, M. Brueggeman, and S. Lipson, "The Remarkable Success of Adaptive Cosine Estimate in Hyperspectral Target Detection", in Proceedings of SPIE, 2013, Vol. 8743, pp.8743012-874302-13

[42] A. Maio, "Fast converging adaptive matched filter and adaptive cosine/coherence estimator", Signal Processing, 2002-10, Vol. 82 (10), pp.1417-1423

[43] E. Truslow, D. Manolakis, M. Pieper, T. Cooley, and M. Brueggeman, "Hyperspectral Performance Prediction of the Adaptive Cosine Estimator", IEEE International Conference on Acoustics, Speech and Signal Processing, 2013, p.6264-6268

[44] J. Harsanyi and C. Chang, "Hyperspectral Image Classification and Dimensionality Reduction: An Orthogonal Subspace Projection Approach", IEEE Transactions on Geoscience and Remote Sensing, 1994-07, Vol. 32 (4), p.779-785

[45] A. Hayden, E. Niple, and B. Boyce, "Determination of trace-gas amounts in plumes by the use of orthogonal digital filtering of thermal-emission spectra," *Appl. Opt.*, vol. 35, no. 16, pp. 2802-2809, 1996, doi: 10.1364/AO.35.002802.

[46] H. Martens and T. Næs, *Multivariate calibration*, 2nd ed., Chichester, John Wiley & Sons, 1989, ISBN: 0 471 90979 3.

[47] J. M. Roger, F. Chauchard, and V. Bellon-Maurel, "EPO-PLS external parameter orthogonalisation of PLS application to temperature-independent measurement of sugar content of intact fruits", *Chemometr. Intell. Lab.*, vol. 66, no. 2, pp. 191-204, 2003, doi: 10.1016/S0169-7439(03)00051-0.

[48] M. Yalcin, S. Yuksel, A. Koz, "Target detection with LWIR hyperspectral scene transfer based on deep learning", IEEE International Geoscience and Remote Sensing Symposium, 2024, p. 7986-7990

[49] J. Martin, "Target Detection Using Artificial Neural Networks on LWIR Hyperspectral Imagery", in Proceedings of SPIE, 2018, Vol. 10644

[50] H. Qin, W. Xie, Y. Li, Q. Du, "HTD-TS3: Weakly Supervised Hyperspectral Target Detection Based on Transformer via Spectral-Spatial Similarity", IEEE Transaction on Neural Networks and Learning Systems, 2023, Vol. PP, p. 1-15

[51] S. Jha, C. Joshi, R. Nidamanuri, "Target Detection in Hyperspectral Imagery Using Atmospheric-Spectral Modeling and Deep Learning", IEEE Geoscience and Remote Sensing Letters", 2022, Vol. 19, p. 1-1

[52] C. C. Funk, J. Theiler, D. A. Roberts, and C. C. Borel, "Clustering to Improve Matched Filter Detection of Weak Gas Plumes in Hyperspectral Thermal Imagery", *IEEE T. Geosci. Remote*, vol. 39, no. 7, pp. 1410-1420, 2001, doi: 10.1109/36.934073.

[53] T. A. Blake et al., "Methods for quantitative infrared directional-hemispherical and diffuse reflectance measurements using an FTIR and a commercial integrating sphere," *Appl. Opt.,* vol. 57, no. 3, pp. 432-446, 2018, doi: 10.1364/AO.57.000432.

[54] N. B. Gallagher, J. M. Shaver, R. Bishop, R. T. Roginski, and B. M. Wise, “Decompositions with Maximum Signal Factors,” *J. Chemometr.*, vol. 28, no. 8, pp. 663-671, 2014, doi: 10.1002/cem.2634.

[55] T. N. Beiswenger, N. B. Gallagher, T. L. Myers, J. E. Szecsody, R. G. Tonkyn, and Y. F. Su *et al.,* “Identification of Uranium Minerals in Natural U-Bearing Rocks Using Infrared Reflectance Spectroscopy”, *Applied Spectroscopy*, vol. 72, no. 2, pp. 209-224, 2018, doi: 10.1177/0003702817743265.

[56] T. J. Johnson, E. Diaz, K. D. Hughey, T. L. Myers, T. A. Blake, and A.C. Dohnalkova *et al.,* “Infrared Optical Constants from Pressed Pellets of Powders: I. Improved n and k Values of (NH4)2SO4 from Single-Angle Reflectance”, *Applied Spectroscopy*, vol. 74, no. 8, pp. 851-867, 2020-08, doi: 10.1177/0003702820930009.

[57] T. L. Myers, C. S. Brauer, and Y. F. Su *et al*., "Quantitative reflectance spectra of solid powders as a function of particle size," *Appl. Opt.*, vol. 54, pp. 4863-4875, 2015.

[58] B. E. Bernacki, T. J. Johnson, and T. L. Myers, "Modeling thin layers of analytes on substrates for spectral analysis: use of solid/liquid n and k values to model reflectance spectra," *Opt. Eng.*, vol. 59, p. 092005, 2020.

[59] T. J. Johnson, L. E. Sweet, and D. E. Meier *et al.*, "Time-Resolved Infrared Reflectance Studies of the Dehydration-Induced Transformation of Uranyl Nitrate Hexahydrate to the Trihydrate Form," *J. Phys. Chem. A*, vol. 119, pp. 9996-10006, 2015.

[60] R. F. Kokaly, R. N. Clark, and G. A. Swayze *et al*., "USGS Spectral Library Version 7," Data Series, 1035 (USGS, Reston, VA, 2017).

[61] L. Mandon, P. Beck, and C. Quantin-Nataf *et al.*, "ROMA: A Database of Rock Reflectance Spectra for Martian In Situ Exploration," *Earth and Space Sci.*, vol. 9, no. 1, p. e2021EA001871, 2022.

[62] B. M. DeVetter, T. L. Myers, and B. D. Cannon *et al.*, "Optical and Chemical Characterization of Uranium Dioxide (UO(2)) and Uraninite Mineral: Calculation of the Fundamental Optical Constants," *J. Phys. Chem. A*, vol. 122, pp. 7062-7070, 2018.

[63] T. L. Myers, T. A. Blake, and M. O. Yokosuk *et al*., "Improved Infrared Optical Constants from Pressed Pellets: II. Ellipsometric n and k Values for Ammonium Sulfate with Variability Analysis," *Appl. Spectrosc.*, vol. 74, pp. 868-882, 2020.

[64] G. Fortin, "Calculation of Spectral Optical Constants Using Combined Ellipsometric and Reflectance Methods for Smooth and Rough Bulk Samples," *Appl. Spectrosc.*, vol. 75, pp. 1449-1460, 2021.

[65] M. O. Yokosuk, T. E. Tiwald, and D. L. Saunders *et al.*, "Combining spectroscopic techniques to determine the optical constants of powdered lactose," *Appl. Opt.*, vol. 60, pp. 2412-2421, 2021.

[66] T. J. Johnson, F. G. Wienhold, J. P. Burrows, G. W. Harris, and H. Burkhard, “Measurements of line strengths in the HO_2 υ_1 Overtone Band at 1.5 μm Using an InGaAsP Laser,” *J. Phys. Chem.*, vol. 95, pp. 6499-6502, 1991.

[67] P. H. C Eilers and H. F. M. Boelens, “Baseline correction with asymmetric least squares smoothing,” *Leiden University Medical Centre Report* 1 (1), 5 468, 2005.

[68] P. H. C. Eilers, “A Perfect Smoother,” *Anal. Chem.*, vol. 75, pp. 3631-3636, 2003, doi: 10.1021/ac034173t.

[69] K. A. Peterson, R. M. Francis, C. A. Banach, A. M. Bradley, S. D. Burton, and J. D. Erickson *et al.,* “Method to derive the infrared complex refractive indices n(λ) and k(λ) for organic solids from KBr pellet absorption measurements”, *Applied Optics*, vol. 63, no. 5, 2024, doi: 10.1364/AO.514661.

[70] A. de Juan and R. Tauler, “Multivariate Curve Resolution: 50 years addressing the mixture analysis problem - A review,” *Anal. Chim. Acta*, vol. 1145, pp. 59-78, 2021, doi: 10.1016/j.aca.2020.10.051.

[71] A. de Juan, J. Jaumot, and R. Tauler, “Multivariate Curve Resolution (MCR). Solving the mixture analysis problem,” *Anal. Methods*, vol. 6, pp. 4964-4976, 2014, doi: 10.1039/C4AY00571F.

[72] N. B. Gallagher, D. O’Sullivan, and M. Palacios “The Effect of Data Centering on PCA Models,” white paper, 2020, doi: 10.13140/RG.2.2.30405.83689.

[73] J. E. Jackson and G. S. Mudholkar, “Control Procedures for Residuals Associated with Principal Component Analysis,” *Technometrics*, vol. 21, no. 3, pp. 341−349, 1979, doi: 10.2307/1267757.

[74] B. M. Wise and N. B. Gallagher, “The process chemometrics approach to chemical process monitoring and fault detection,” *J. Process Control.*, vol. 6, no. 6, pp. 329-348, 1996, doi: 10.1016/0959-1524(96)00009-1.

[75] Mathworks, Natick, MA

[76] Eigenvector Research, Inc, Manson, WA USA

[77] A. Savitzky and M. J. E. Golay "Smoothing and Differentiation of Data by Simplified Least Squares Procedures," *Anal. Chem.,* vol. 36, no. 8, pp. 1627-1639, 1964.

[78] NOAA Sunrise/Sunset Calculator, accessed April 2024, https://gml.noaa.gov/grad/solcalc/sunrise.html

[79] Weather Underground historical data, accessed January 2024, https://www.wunderground.com/history/daily/us/wa/richland/KPSC/date/2017-10-4

[80] R. Lindenmaier, S. Williams, R. Sams, and T. Johnson, “Quantitative Infrared Absorption Spectra and Vibrational Assignments of Crotonaldehyde and Methyl Vinyl Ketone Using Gas-Phase Mid-Infrared, Far-Infrared, and Liquid Raman Spectra: s-cis vs s-trans Composition Confirmed via Temperature Studies and ab Initio Methods”, J. Physical Chemistry A, 2017-02, Vol. 121(6), p. 1195-1212

[81] S. Williams, T. Johnson, S. Sharpe, V. Yavelak, R. Oates, and C. Brauer, “Quantitative vapor-phase IR intensities and DFT computations to predict absolute IR spectra based on molecular structures: I Alkanes”, Journal of Quantitative Spectroscopy and Radiative Transfer, 2013-11, Vol 129, p. 298-307